$O(^1D)$ Branching Fraction from the Reaction $N(^2D) + O_2 \rightarrow NO(^2\Pi,v,J) + O(^3P,^1D)$

Steven M. Miller* and Martin Hunter†

Space Vehicles Directorate, Air Force Research Laboratory, AFRL/VSBYM, Hanscom Air Force Base,
29 Randolph Road, Bedford, Massachusetts 01731-3010

Received: December 16, 2003; In Final Form: April 5, 2004

The reaction $N(^2D) + O_2 \rightarrow NO(^2\Pi,v,J) + O(^3P,^1D)$ has been considered for many years as a possible source of $O(^1D)$ in the thermosphere. We have used the Cold Chemical Infrared Simulation Experiment (COCHISE) facility to determine an upper limit to the $O(^1D)$ branching fraction of this reaction by observing the absence of the radiative decay of $O(^1D)$ and $O_2(b^1\Sigma)$ produced by efficient energy exchange with O_2. By carefully modeling the kinetic and fluid dynamics of the experiment, an upper limit of 0.02 ± 0.02 was found for the branching fraction into the $O(^1D)$ product channel.

I. Introduction

$O(^1D)$ is a long-lived radiator ($\tau = 148$ s at 630 nm) in the thermosphere. This long radiative lifetime allows most of the $O(^1D)$ electronic energy to be transferred to other thermospheric species, such as N_2 and O_2, to create $N_2(v)$, which does not radiate, and $O_2(b^1\Sigma)$ which possesses a shorter lifetime ($\tau = 12$ s) and radiates in the near-infrared region at 760−765 nm. Observations of $O(^1D)$ radiance have been used extensively to measure both the temperature of the thermosphere and thermospheric wind velocities. There has been an ongoing controversy during the past 20 years, in regard to the source of this important thermospheric species. The original source, which was suggested in 1979 by Sharp et al.,[1] is the dissociative recombination of O_2^+:

$$O_2^+ + e^- \rightarrow O(^1D) + O \qquad (1)$$

This reaction is well-accepted as the main source of thermospheric $O(^1D)$. Several aeronomers[2,3] have claimed that this dissociative recombination source cannot account for all of the 630.0 nm radiation observed. This conclusion was based on the analysis of rocket and satellite data. However, others[4] have interpreted that same rocket data, and data from similar campaigns, in such a way that all of the 630.0 nm radiance can be accounted for by the aforementioned reaction. Those whose analysis has implied a missing source of $O(^1D)$ have relied on the reaction

$$N(^2D) + O_2 \rightarrow NO(^2\Pi,v,J) + O(^3P,^1D) \qquad (2)$$

to produce the additional $O(^1D)$. Support for this second source came from papers by Kennealy et al.[5] in 1979 and Rawlins et al.[6] in 1989, which described laboratory studies of reaction 2 and the resulting product distribution of NO(v,J). Those laboratory studies concluded, using the indirect evidence of a break in the nitric oxide product ground-state vibrational distribution at $v = 8$, that the branching ratio for producing $O(^1D)/O(^3P)$ from reaction 2 was ~70%. This result was then used by the aeronomers whose models required additional $O(^1D)$ as evidence of a second source of $O(^1D)$.

We have modified the Cold Chemical Infrared Simulation Experiment, or COCHISE, which is the same apparatus that Kennealy and Rawlins used, to extend its spectral range from the infrared into the visible and near-ultraviolet. We then carefully measured emission at 630.0 nm for evidence of $O(^1D)$ product of reaction 2. Because $O(^1D)$ possesses a very long radiative lifetime (148 s) and, therefore, is difficult to detect, we also used the 0−0 band emission at 760−765 nm from the $O_2(b^1\Sigma)$ product of the additional energy transfer mechanism

$$O(^1D) + O_2 \rightarrow O(^3P) + O_2(b^1\Sigma) \qquad (3)$$

as a tracer.

A model of the COCHISE flow and reaction kinetics was developed and is presented in the appendix of this paper. Using this model and the calibration results, the upper limit detection thresholds for $O(^1D)$ and $O_2(b^1\Sigma)$ signals were calculated and the best-fit upper limit branching ratio for reaction 2 is found.

II. Experimental Section

The COCHISE facility is well-described by the 1984 article by Rawlins et al.[7] Only the modifications relevant to this work will be described here. A fiber-optic bundle was designed with cryogenic feed-throughs so that both infrared (IR) and visible (vis) emission could be detected simultaneously (see Figure 1). Fused silica fiber was chosen, because of its low loss in the visible range and its lack of transmission in the IR range. This ensured that no room-temperature IR background would leak into the chamber through the fiber-optic material. The fiber bundle is comprised of 80 100-μm-diameter fibers, each with a numerical aperture of 0.22. The internal end of the bundle is a close-packed cylinder that collects light focused from the reaction chamber by a 2.54-cm-diameter spherical fused silica lens. At the external end, the fibers are all placed in a line, 100 μm in diameter by 1 cm in length. This provides particularly efficient coupling into a 0.5-m CVI model 480 monochromator

---

* Author to whom correspondence should be addressed. Telephone: (781)-377-2807. Fax: (781)-377-8900. E-mail address: steven.miller@hanscom.af.mil.

† Now with G. R. Harrison Spectroscopy Laboratory, Massachusetts Institute of Technology, Cambridge, MA 02139.

10.1021/jp031340k CCC: $27.50

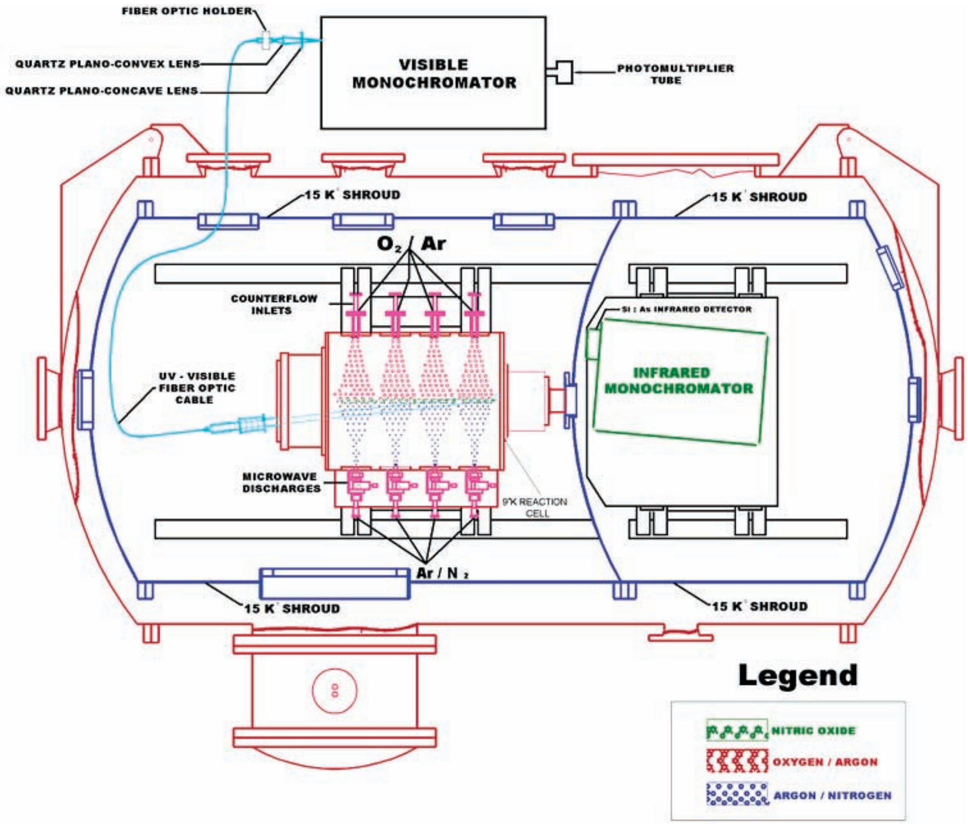

Figure 1. Schematic diagram of the Cold Chemical Infrared Simulation Experiment (COCHISE). Facility shown with added fiber optics for visible spectroscopy.

via a simple two-lens system. One lens is matched to the numerical aperture of the fiber bundle, and one is matched to the numerical aperture of the monochromator, 0.064. The lenses magnify the 100-μm-wide fiber bundle by 2.5 to produce an image of the bundle 2.5 cm by 250 μm on the entrance slit of the monochromator. This matches well to the entrance slit dimensions of 2.5 cm × 250 μm, which provides a spectral resolution of 0.4 nm. The light exiting the monochromator is collected by an additional lens and focused onto a Hamamatsu model R943-2 photomultiplier tube encased in a Products-for-Research model TE182TSRF housing cooled to −23 °C. The signal is then amplified by an SRS model SR445 fast preamplifier and connected to an SR430 multichannel averager. A LabVIEW 5.1 program running under Windows NT 4.0 on a Pentium-based personal computer (PC) collects the output of the averager. At the same time, the IR emission is collected through a cryogenic IR monochromator onto a Si:As detector. The detector signal is fed into a cold preamplifier and onto an SRS model SR530 lock-in amplifier. A LabVIEW program running on a second PC collects the output of the lock-in amplifier.

To gain additional sensitivity to the visible chemiluminescence of $O(^1D)$ and $O_2(b^1\Sigma)$, a series of experiments were performed by providing a window and lens directly into the reaction chamber (Figure 2). Although this precludes the use of IR spectroscopy during these runs, the IR chemiluminescence has been well-characterized from many previous experiments under the same conditions.

Sensitivity analysis of the COCHISE kinetic modeling (Section V) demonstrates that the concentration of $O(^1D)$ and $O_2(b^1\Sigma)$ in the center of the reaction chamber is highly sensitive to the total pressure there. Therefore, we used several instruments to measure the pressure in this region. These included Granville Phillips model 275 mini-convectron gauges, an MKS Instruments model 120AA-000 RAJ Baratron gauge, and a Varian model 580 nude Bayard-Alpert type ionization gauge tube. The convectron gauge is the least accurate and is used to monitor the pressure in the inlet ports as well as major fluctuations in the reaction cell pressure. The ionization gauge is significantly more accurate but cannot be used during data collection, because of its bright visible emission during operation. Thus, the Baratron monitored the pressure during data collection and direct comparisons were made to the nude ionization gauge before and after each run. The disparity between the readings of these gauges was never greater than 30% for experiments contributing to these results.

The study was comprised of three parts. First, the visible optical path and detection system—both via fiber and direct detection—were calibrated. Second, the sensitivity with which $O(^1D)$ and $O_2(b^1\Sigma)$ can be detected in COCHISE was determined. And, finally, the visible signal from $O(^1D)$ and $O_2(b^1\Sigma)$ from the reaction of $N(^2D)$ with O_2 in the COCHISE reaction chamber was measured.

The calibration of the optical systems was performed before and after each experimental run. An Optronics Laboratory model 220IR standard spectral NIST traceable reference lamp and power supply were used for all calibrations. To reduce the intensity of the lamp sufficiently to fall within the dynamic range of the photomultiplier tube, two reflective Melles Griot neutral density filters with known calibration curves were used. Care was taken to remove all scattering surfaces during calibration. The geometry and gas flows of the COCHISE reaction cell, as shown in Figure 1, create a stagnation zone such that all product species are made within a 50-cm-long cylinder with a radius of

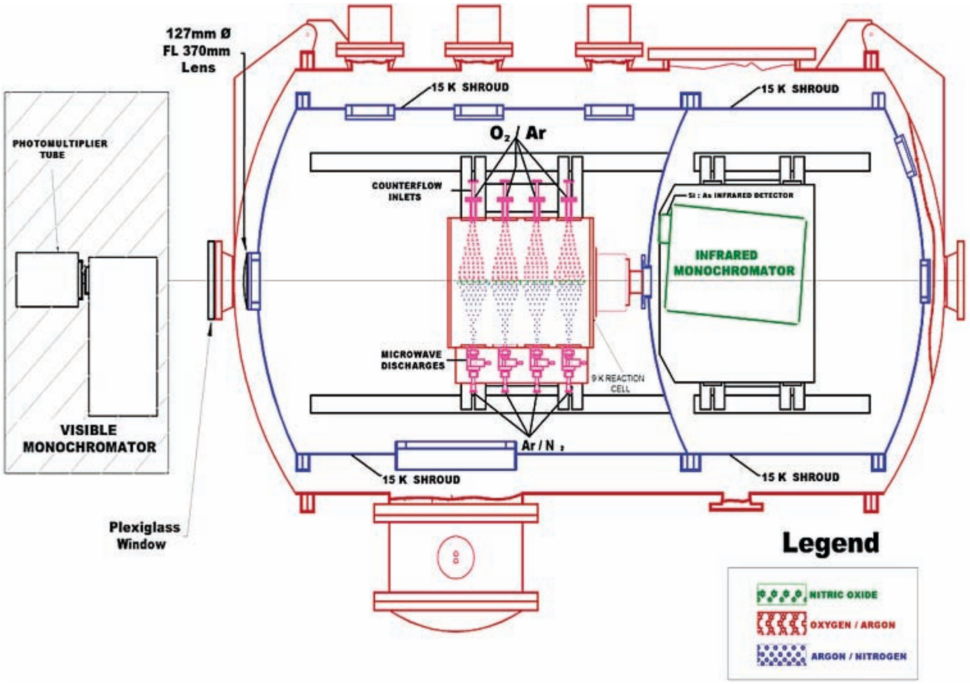

Figure 2. COCHISE adapted for the detection of direct visible emission from the reaction zone. Under these conditions, the 300 K blackbody light leaking in through the coupling window prohibits the infrared detection of gas-phase products.

TABLE 1: COCHISE Optical Collection Efficiencies

	fiber-optic collection	direct optical collection via 5 in. lens
solid angle efficiency, ϵ_Ω[a]	1.5×10^{-4}	6.7×10^{-4}
light collection efficiency, ϵ_0[b]	1.9×10^{-3}	1.42×10^{-1}
collection volume, *V*	6.3 cm^3	7.7 cm^3

[a] ϵ_Ω represents the efficiency as a result of the effective solid angle of light collection. [b] ϵ_0 represents the efficiency of light collected by the optical path.

9 cm. The solid angle and imaging of the optical system collects light from a cone-shaped volume within the reaction zone of 6.3 cm^3 for the fiber-optic collection and 7.7 cm^3 for the direct collection configuration. All calibrations were performed using the same optical path as the experimental observations. Systematic errors in the calibration (e.g., alignment, aging of the lamp filament, and photomultiplier tube temperature) are estimated to be ~30%. The calibrations gave the collection efficiencies shown in Table 1, where ϵ_Ω represents the solid angle over which light is collected and ϵ_0 represents the efficiency of the optical collection system from the first collection lens to the output of the discriminator.

The long fluorescence lifetime (148 s), low nascent densities, and fast quenching by O_2 in this set of experiments combine to make it very difficult to observe $O(^1D)$ directly at 630.0 nm. The fast and efficient[8] quenching of $O(^1D)$ by O_2 (4.0×10^{-11} cm^2 molecule^{-1} s^{-1} at room temperature) to produce $O_2(b^1\Sigma)$ provides an excellent tracer of the $O(^1D)$, because O_2 is a factor of 100 more abundant than its next-fastest quencher, N_2 (2.6×10^{-11} cm^2 molecule^{-1} s^{-1}), in our experiments. We calibrated the sensitivity of COCHISE to $O_2(b^1\Sigma)$ by performing a separate experiment, which consisted of an argon microwave discharge with varying mole fractions of oxygen while counterflowing pure argon. Although there are potentially several mechanisms for the production of $O_2(b^1\Sigma)$ from a discharge, the main one follows from the dissociative recombination of ionized oxygen molecules, which produces $O(^1D)$ that is subsequently quenched by O_2.

The third experimental portion of this study involved the measurement of the $O(^1D)/O_2(b^1\Sigma)$ concentrations produced by reaction 2. The experimental conditions in the reaction zone are similar to those used in previous measurements of the NO vibrational distribution from this reaction:[6,9] a 10% mole fraction of nitrogen in an argon discharge opposed to a pure oxygen counterflow. In the present study, only a 1% mole fraction of nitrogen was used to limit $O(^1D)$ quenching by N_2. A total of 700 μmol/s of argon was flowed through each of the four discharges and a momentum balance of 560 μmoles of oxygen was flowed through each of the counterflow inlets. It was found previously[6] that under these conditions, NO is produced from this reaction at a concentration level of 3×10^9 cm^{-3} in the field of view. Spectra were taken at both the 630 nm wavelength region of $O(^1D)$ emission and at the 765 nm wavelength region of $O_2(b^1\Sigma)$ emission. This experiment was performed using both fiber-optic collection conditions (Figure 1) and direct lens collection conditions (Figure 2).

III. Experimental Results

1. $O_2(b^1\Sigma)$ Detection Sensitivity. After thorough intensity calibration of the collection optics, measurement of the $O_2(b^1\Sigma)$ detection sensitivity was performed as described in Section II. The $O(^1D)$ made in the high-pressure (1 Torr) sidearm from a discharge of an oxygen and argon mixture is rapidly quenched by O_2 to $O_2(b^1\Sigma)$. $O_2(b^1\Sigma, v > 0)$ is quenched further as it flows to the center of the reaction cell. Here, emission from the $O_2(b^1\Sigma)$ is monitored. With a high mole fraction (33%) of oxygen in an argon buffer, in the discharge, emission from the $O_2(b^1\Sigma)$ electronic state to the $O_2(X,^3\Sigma)$ ground state can clearly be observed in Figure 3.

Along with the $O_2(b^1\Sigma)$ emission, this spectral band contains line emission from Ar and O atoms. The NIST Atomic Spectra Database[10] was used to identify these atomic lines and these line positions were, in turn, used to calibrate the experimental data spectrally. Many metastable levels of argon are directly

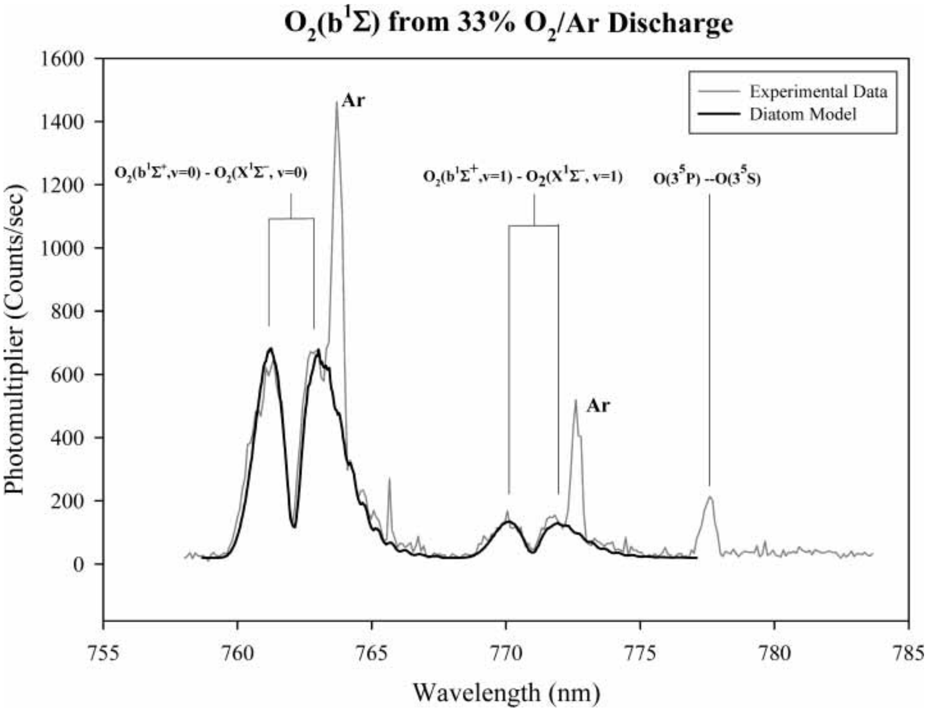

Figure 3. Emission in the COCHISE reaction chamber from products originating in a 33% O_2/Ar discharge in the sidearm. The thin gray line is the experimental data and the dark thick line represents a two-temperature (100 and 200 K) fit to the $O_2(b^1\Sigma)$ emission. The fit contains a 70% relative contribution from the $O_2(b^1\Sigma)$ (0,0) band at 100 K, a 30% relative contribution from the $O_2(b^1\Sigma,0,0)$ band at 200 K, a 12% relative contribution from the $O_2(b^1\Sigma,1,1)$ band at 100 K and a 5% relative contribution from the $O_2(b^1\Sigma,1,1)$ band at 200 K. The Ar lines observed were used to spectrally calibrate the emission. These data were taken using the fiber-optic optical path.

excited by the microwave discharge. As these atoms relax, the resulting cascade, through the atomic levels, results in line emission at various wavelengths from the ultraviolet (UV) region through the IR region. The O atom lines are emission from the 3^5P state to the 3^5S of neutral oxygen. The microwave discharge ionizes oxygen molecules to produce O_2^+. The O_2^+ then undergoes dissociative recombination to produce O atoms. Some of these O atoms are excited to high-lying Rydberg states via collisional energy exchange with metastable Ar atoms. These long-lived Rydberg atoms are then transported to the reaction cell, by which time they have relaxed to the triplet ^5P state of oxygen from which they promptly radiate at 777.5 nm. Note that, although ions are precursors to the production of these O atoms, the higher pressures (1−2 Torr) in the sidearms cause recombination of the ions before they enter the reaction cell.

DIATOM,[11] which is a diatomic modeling program that handles non-allowed transitions well, was used to model the $O_2(b^1\Sigma)$ spectral data. The results of this modeling were fit to the data. This is shown as the bold lines in Figures 3 and 4. The fitting parameters were the intensity of each band $O_2(b^1\Sigma_g^+,v = 0) \rightarrow O_2(X^3\Sigma_g^-,v = 0)$ and $O_2(b^1\Sigma_g^+,v = 1) \rightarrow O_2(X^3\Sigma_g^-,v = 1)$ and the rotational temperature. The best fit to the data shown in Figure 3 requires two rotational temperatures: 100 and 200 K. The $O_2(b^1\Sigma)$ state molecules are formed in the discharge sidearm at a higher temperature and are cooled during the supersonic expansion into the reaction cell (see Figure A1 in the Appendix) and then begin an equilibration process in the stagnation region. The two-temperature fit represents an ensemble of molecules that have been thermalized together with a component that has yet to be fully equilibrated. The mole fraction of O_2 in the discharge was then reduced to 3%, to determine the detection threshold for $O_2(b^1\Sigma)$, and the results are shown in Figure 4. The signal-to-noise ratio of the $O_2(b^1\Sigma_g^+,v = 0) \rightarrow O_2(b^3\Sigma_g^-,v = 0)$ emission is 6:1. Thus, this signal is approximately a factor of 6 above the threshold of detection.

TABLE 2: COCHISE Detection Thresholds of $[O(^1D)]$ and $[O_2(b^1\Sigma)]$ for Both Fiber-Optic and Direct Optic Collection, Assuming a Signal-to-Noise Ratio of 2

	$[O(^1D)]$	$[O_2(b^1\Sigma)]$
ρ_{fiber}	2.8×10^9 cm^{-3}	1.9×10^8 cm^{-3}
ρ_{direct}	3.3×10^8 cm^{-3}	2.2×10^7 cm^{-3}

The number density of the emitting molecules in the field of view can be calculated using the efficiencies from Table 1 and the integrated count rate as follows:

$$\rho = \frac{I\tau}{\Delta\lambda\epsilon_0\epsilon_\Omega V} \tag{4}$$

where ρ is the number density of emitting molecules in the field of view, I the integrated count rate, τ the fluorescence lifetime of $O_2(b^1\Sigma)$ (12 s), $\Delta\lambda$ the resolution of the monochromator (250 μm slits, 0.4 nm) used, and V the reaction zone volume sampled by the collection optics from Table 1. For these conditions, the detection thresholds are shown in Table 2.

Results from $N(^2D) + O_2$ Experiments. No $O(^1D)$ signal was ever observed using either fiber-optic or direct optical collection. This is not at all surprising, because of both the long radiative lifetime of $O(^1D)$ and the relatively high detection thresholds of Table 2. Upper limits on the production of $O_2(b^1\Sigma)$ in the reaction volume from reaction 1 can be determined using the spectral scans of both the fiber-optic collection and the direct lens collection optical paths (Figures 5 and 6). Clearly, there is no detectable signal using the fiber-optic collection method, Figure 5. There is no clear evidence for $O_2(b^1\Sigma)$ emission in the direct lens collection experiments either, although if one

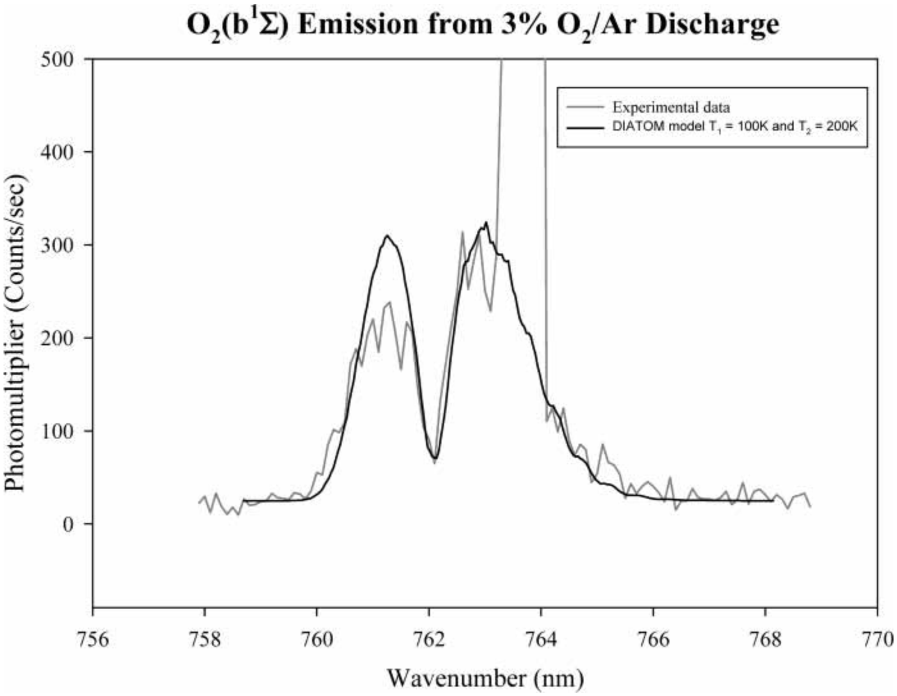

Figure 4. Emission in the COCHISE reaction chamber from products originating in a 3% O_2/Ar discharge in the sidearm. The thin gray line is the experimental data and the dark thick line represents a fit to the $O_2(b^1\Sigma)$ emission using DIATOM. These data were taken using the fiber-optic optical path.

TABLE 3: Parameters for Chemical Dynamics Model Fit to COCHISE Data[a]

parameter	value
pressure	4 mTorr
temperature	100 K
$N(^2D) + O_2$ reaction rate	4×10^{-12} cm^3 molecule^{-1} s^{-1}
$O(^1D) + O_2$ quenching rate	2.5×10^{-11} cm^3 molecule^{-1} s^{-1}
diffusion coefficients	see Table A2 in the Appendix
mole fraction of $N(^2D)$ in discharge	4×10^{-5}
branching fraction to $O(^1D)$ product	floating variable

[a] Values reflect the COCHISE experimental conditions.

uses the differential signals of Figures 5 and 6 at 762.3 nm as a possible indication of $O_2(b^1\Sigma)$ emission, then an upper limit on the $O_2(b^1\Sigma)$ concentration can be calculated using eq 4. The mean differential signal—3000 counts/s at a signal-to-noise ratio of 2—indicates a $[O_2(b^1\Sigma)]$ of $<5 \times 10^7$ cm^{-3} in the reaction zone. The modeling results of the next two sections will determine the best-fit upper limit branching ratio and its error.

IV. Fit to Chemical Dynamics Model

The chemical dynamics model, which is described in the appendix, was run with all inputs fixed except for the branching fraction of reaction 2. The most significant parameters are shown in Table 3.

The pressure and temperature were those measured experimentally. The rate coefficient used for $N(^2D) + O_2$ was a taken from the experimentally determined temperature-dependent coefficients of Slanger et al.[12] evaluated at 100 K (4.0×10^{-12} cm^3 molecule^{-1} s^{-1}). The room-temperature rate coefficient for the quenching of $O(^1D)$ by O_2 is $k = 4.0 \times 10^{-11}$ cm^3 molecule^{-1} s^{-1}.[8] The reaction has a very weak negative temperature dependence, and its expected value at COCHISE operating temperatures lies in the range of $k(100\text{ K}) = 0.2 \times 10^{-10}-1.8 \times 10^{-10}$ cm^3 molecule^{-1} s^{-1}.[13] Our models use a lower-end value of 2.5×10^{-11} cm^3 molecule^{-1} s^{-1} for this reaction, to avoid overpredicting the $[O_2(b^1\Sigma)]$ that is expected.

Fitting the model to the data produces an upper limit on the branching fraction of reaction 2 to $O(^1D)$ of 0.02, which is significantly below the previously reported value of 0.76. To determine the potential error in this result, an analysis of the sensitivity of the model to the major parameters was performed.

V. Sensitivity Analysis

Because of the complexity of the fluid/kinetic model described in the appendix, it is prudent to characterize which small changes in parameters cause the greatest changes in $[O_2(b^1\Sigma)]$ and $[O(^1D)]$.

The first test for the model's accuracy in representing the dynamics in the COCHISE reaction zone is to determine whether it can reproduce the measured steady-state pressure (P) under typical experimental conditions ($T = 100$ K and $M = 0.027$ g Ar/s). The measured pressure ($P = 4$ mTorr) is used to define the reaction zone cylindrical radius (r_{RZ}) via eq 5. After the reaction zone geometry is established, a simplified master equation is constructed that involves only the formation and loss processes of the argon carrier gas, as described in the appendix. The equation is solved numerically for the steady-state argon density, which can then be compared to the experimentally measured value.

The result of this test indicates that our model slightly underestimates the steady-state pressures in COCHISE experiments (by ~20%). The good agreement is notable, considering that the test does not involve optimization of any adjustable parameters. To correct for the slight density underestimation, however, we decided to treat the carrier gas source term as an adjustable parameter (see Appendix).

An important consideration is the concentration of $N(^2D)$ and $N(^2P)$ made in the discharge and transported to the reaction cell. Inputs to the model include a mole fraction of 3×10^{-5} of $N(^2D)$ and a mole fraction of $N(^2P)$ that is a factor of 4 less than this value,[6] both consistent with the [NO] observed in the

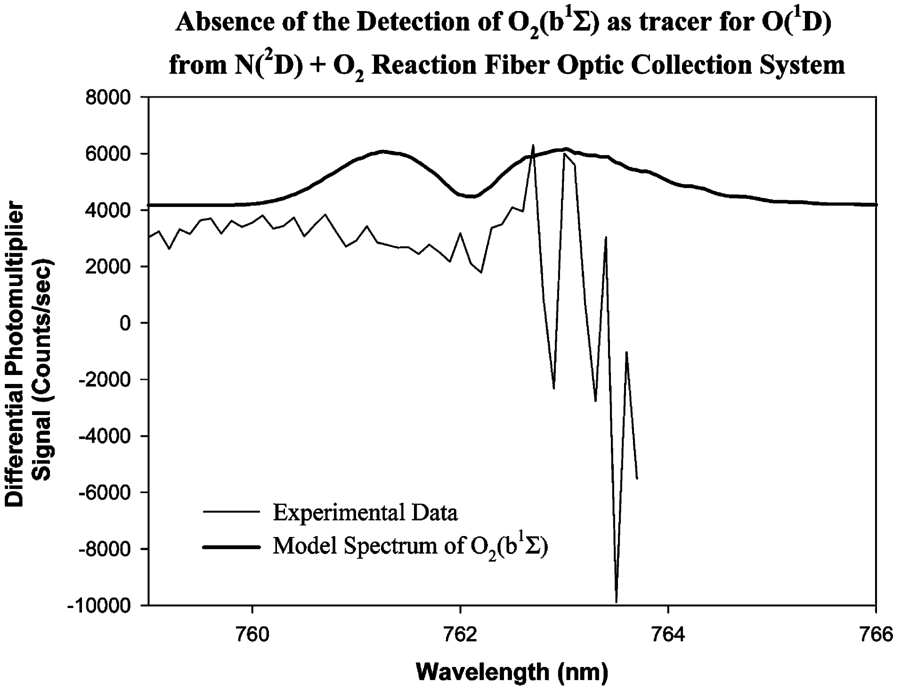

Figure 5. O$_2$(b$^1\Sigma$,v = 0) spectral region using fiber-optic collection. The experimental data curve is the difference between an averaged co-added set of monochromator scans with a pure O$_2$ counterflow and a scan with a pure argon counterflow (no in situ production of O(1D)/O$_2$(b$^1\Sigma$) possible). The calculated model spectrum of O$_2$(b$^1\Sigma$,v = 0) is shown for spectral reference. The larger noise at wavelengths >762.5 nm is due to the differential nature of the experimental curve (the difference of large numbers under the Ar line).

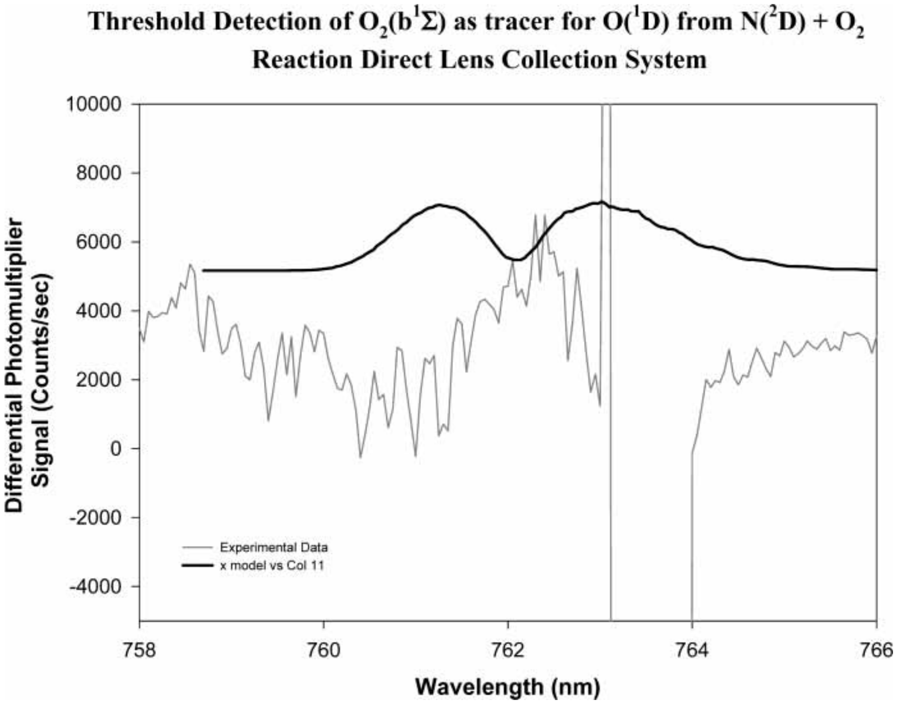

Figure 6. O$_2$(b$^1\Sigma$,0,0) band spectral region via direct optical collection by lens. The experimental data curve is the difference between a spectrum taken with a pure O$_2$ counterflow and a scan taken with a pure Ar counterflow (no in situ production of O(1D)/O$_2$(b$^1\Sigma$) possible). The calculated model spectrum of O$_2$(b$^1\Sigma$,0,0) band is shown for spectral reference. The larger noise and negative signal at wavelengths >762.5 nm is due to the differential nature of the experimental curve (the difference of large numbers under the Ar line).

reaction cell and literature values. Although there are no published articles demonstrating the production of NO + O from the reaction of N(^{2}P) + O$_2$, one can use the published quenching rate of N(^{2}P) by O$_2$,[14] 1.8×10^{-12}, together with the concentrations used previously to determine that any production of O(^{1}D) by N(^{2}P) + O$_2$ will be at least an order of magnitude lower than that produced by reaction 2.

The results of the kinetic model sensitivity testing show strong changes to the O(^{1}D) and O$_2$(b$^1\Sigma$) densities as a function of pressure, temperature, mole fraction of N(^{2}D), and the O$_2$ quenching rate of O(^{1}D). As can be seen in Figures 7 and 8, both [O(^{1}D)] and [O$_2$(b$^1\Sigma$)] are very sensitive to the pressure in the center of the reaction cell. Within our measured operating range of $P = 4 \pm 0.2$ mTorr in COCHISE experiments,

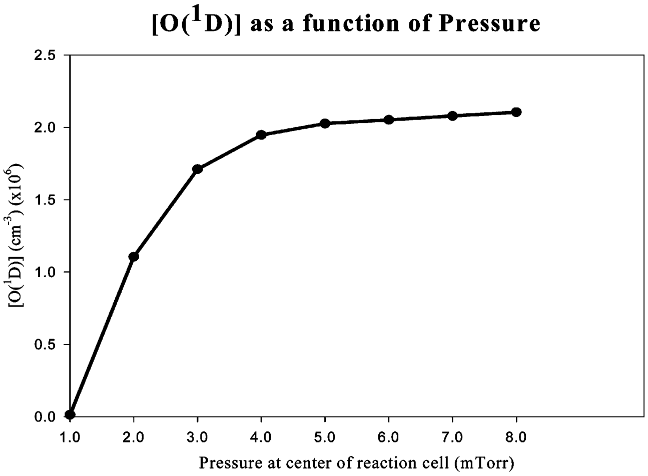

Figure 7. Pressure dependence of [O(^{1}D)]. Conditions for this model run were as follows: a reaction zone temperature of 100 K, an N(^{2}D) mole fraction of 4×10^{-5}, and a quenching rate coefficient of 2.5×10^{-11} cm^3 molecule^{-1} s^{-1} for the quenching of O(^{1}D) by O_2.

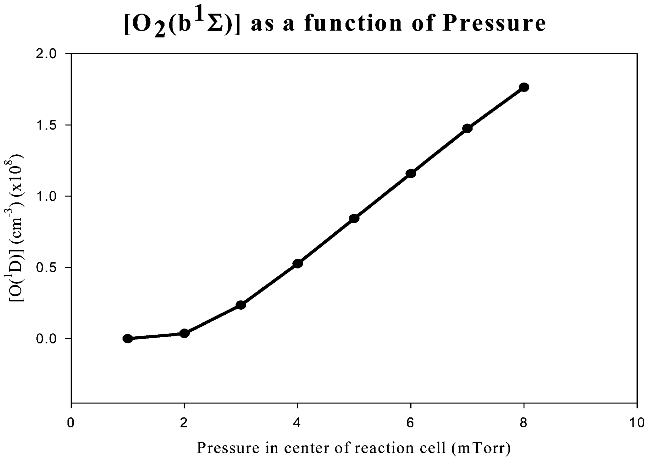

Figure 8. Pressure dependence of [O_2(b$^1\Sigma$)]. Conditions for this model run were as follows: a reaction zone temperature of 100 K, an N(^{2}D) mole fraction of 4×10^{-5}, and a quenching rate coefficient of 2.5×10^{-11} cm^3 molecule^{-1} s^{-1} for the quenching of O(^{1}D) by O_2.

however, the corresponding uncertainties in [O(^{1}D)] and [O_2(b$^1\Sigma$)] are expected to be only 5% and 10%, respectively. Figures 9 and 10 shows that [O_2(b$^1\Sigma$)] decreases as a function of temperature, whereas [O(^{1}D)] is insensitive to temperature for this range of temperature values. As the temperature increases, O(^{1}D) is quenched more slowly because [O_2] is lower. At the same time, the combined diffusion and convection rate increases for O(^{1}D). These offsetting effects result in an apparent insensitivity to temperature in Figure 9. For the same conditions, [O_2(b$^1\Sigma$)] decreases because of both lower [O_2] and increased diffusion and convection rates. Thus, Figure 10 displays a decrease as a function of temperature. Experimentally, the lower temperature limit is determined by the ability to flow N_2 through the gas lines. Heating the gas lines to a temperature of <100 K allows solid plugs to develop at cold spots in the lines. The temperature in the reaction zone is accurately monitored by determining the best nonlinear least-squares fit to the NO(v,J) infrared spectra. The measured temperature is typically $T = 100 \pm 5$ °C, corresponding to an uncertainty in predicted [O(^{1}D)] and [O_2(b$^1\Sigma$)] of 2% and 10%, respectively. Although the quenching rate of O(^{1}D) quenched by O_2 is well-established at room temperature, it is likely to be larger at 100 K.[13] The sensitivity test shows the expected result of a reduced [O(^{1}D)] and an enhanced [O_2(b$^1\Sigma$)] (Figures 11 and 12). Because the [O(^{1}D)] is too low to be observed directly under any conditions in COCHISE (see detection limits in Table 2), any increase in quenching rate increases our ability to observe the [O_2(b$^1\Sigma$)]. This is limited, of course, by the depletion of the [O(^{1}D)], which appears as a saturation of the [O_2(b$^1\Sigma$)] in Figure 12.

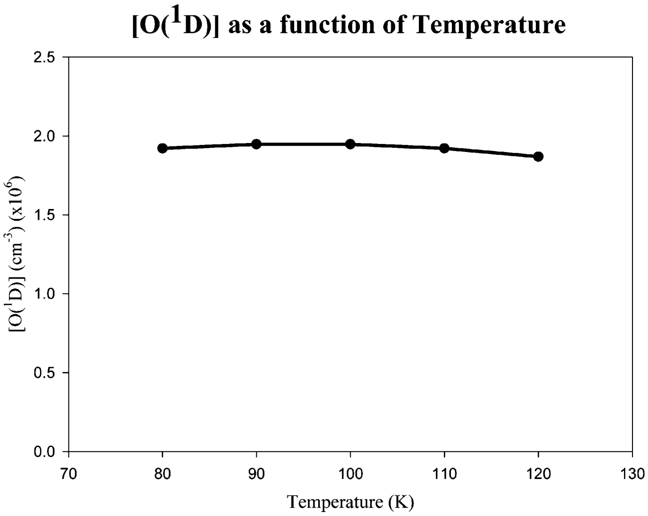

Figure 9. Temperature dependence of [O(^{1}D)]. Conditions for this model run were as follows: a reaction zone pressure of 4 mTorr, an N(^{2}D) mole fraction of 4×10^{-5}, and a quenching rate coefficient of 2.5×10^{-10} cm^3 molecule^{-1} s^{-1} for the quenching of O(^{1}D) by O_2.

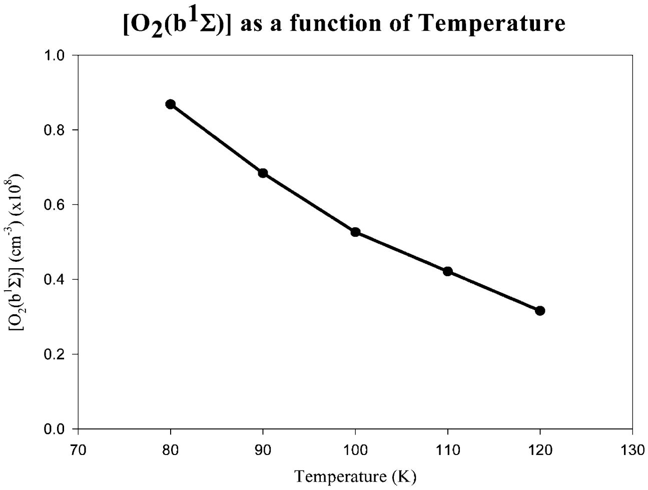

Figure 10. Temperature dependence of [O_2(b$^1\Sigma$)]. Conditions for this model run were as follows: a reaction zone pressure of 4 mTorr, an N(^{2}D) mole fraction of 4×10^{-5}, and a quenching rate coefficient of 2.5×10^{-11} cm^3 molecule^{-1} s^{-1} for the quenching of O(^{1}D) by O_2.

The mole fraction of N(^{2}D) from the discharge is linearly related to the production of O(^{1}D) and O_2(b$^1\Sigma$). Both [O(^{1}D)] and [O_2(b$^1\Sigma$)] vary by a factor of 4, because the mole fraction N(^{2}D) is varied over a factor of 4 in the discharge by varying the mole fraction of N_2 (Figures 13 and 14). Although these figures could be interpreted to imply a large potential variance in the concentrations of O(^{1}D) and O_2(b$^1\Sigma$), experimentally, we obtained an indirect measurement of [N(^{2}D)] separately by monitoring the corresponding [NO] produced from reaction 2.

Finally, Figures 15 and 16 show the sensitivity for the production of [O(^{1}D)] and [O_2(b$^1\Sigma$)] on the diffusion rates of excited atomic species. As described in the Appendix, it is possible that, at high [O_2], the diffusion rates of excited atoms

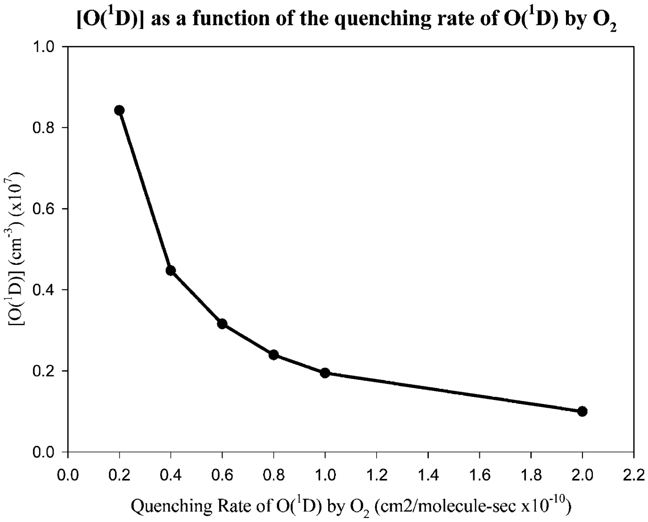

Figure 11. O$_2$ quenching rate dependence of [O(^{1}D)]. Conditions for this model run were as follows: a reaction zone pressure of 4 mTorr, a temperature of 100 K, and an N(^{2}D) mole fraction of 4 × 10^{-5}.

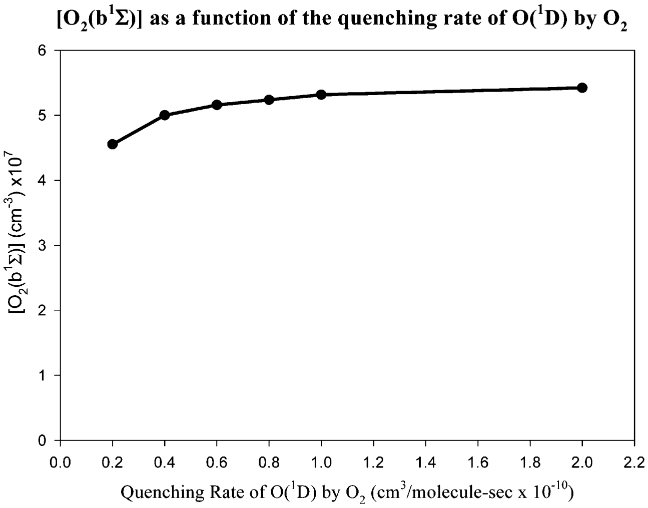

Figure 12. O$_2$ quenching rate dependence of [O$_2$(b$^1\Sigma$)]. Conditions for this model run were as follows: a reaction zone pressure of 4 mTorr, a temperature of 100 K, and an N(^{2}D) mole fraction of 4 × 10^{-5}.

may be reduced. These figures show that any reduced diffusion rates increase the concentrations of O(^{1}D) and O$_2$(b), thus making them more easily detected. In the unlikely event that the diffusion rates for these excited atomic species were to be larger than those used in our model, these figures show that it requires an increase of more than a factor of 3 in diffusion rate to half the [O$_2$(b$^1\Sigma$)].

Table 4 summarizes the sensitivity of the most important parameters in the model. The first column contains the uncertainty to which the parameters were either measured or are known from the literature. The second column contains the resulting uncertainty in the [O$_2$(b$^1\Sigma$)] from the corresponding input from column 1. Clearly, the pressure, temperature, and mole fraction of N(^{2}D) in the discharge are the most sensitive parameters. A conservative error estimate is made by running the model with each parameter of Table 4 set at its extreme uncertainty to produce either the least or the greatest [O$_2$(b$^1\Sigma$)] and, therefore, the smallest and largest values of the branching fraction of reaction 2. The error using this methodology is ±0.02. Although this method probably overstates the error by assuming all variables are at their maximum error in either direction, it is reasonable when considering the 30% error in calibration and difficulty in determining precise systematic errors.

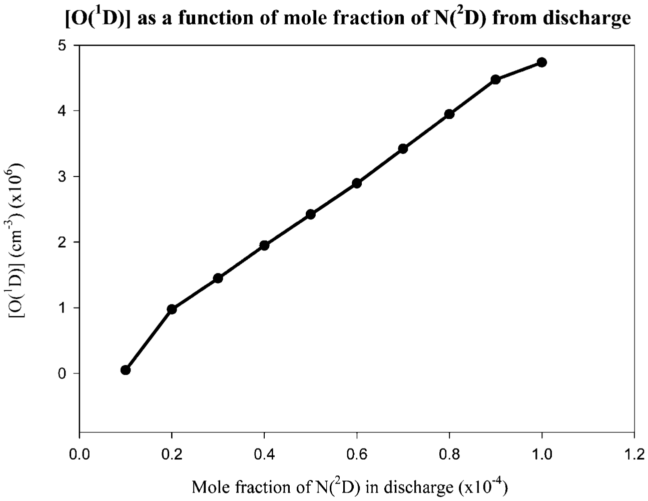

Figure 13. [O(^{1}D)] dependence on [N(^{2}D)]. Conditions for this model run were as follows: a reaction zone pressure of 4 mTorr, a temperature of 100 K, and a quenching rate coefficient of 2.5 × 10^{-11} cm^3 molecule^{-1} s^{-1} for the quenching of O(^{1}D) by O$_2$.

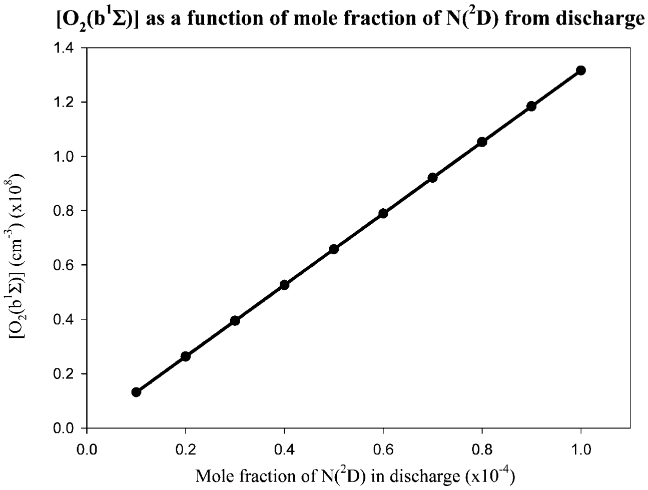

Figure 14. [O$_2$(b$^1\Sigma$)] dependence on [N(^{2}D)]. Conditions for this model run were as follows: a reaction zone pressure of 4 mTorr, a temperature of 100 K, and a quenching rate coefficient of 2.5 × 10^{-11} cm^3 molecule^{-1} s^{-1} for the quenching of O(^{1}D) by O$_2$.

TABLE 4: Uncertainties in [O$_2$(b$^1\Sigma$)] as a Result of Sensitivity Studies Performed on the Listed Parameters in the Kinetic Model

parameter	uncertainty in parameter(%)	range of parameter values	uncertainty in [O$_2$(b$^1\Sigma$)] (%)	range of [O$_2$(b$^1\Sigma$)] values
pressure	±15	3.4−4.6 mTorr	±37	$3.0 \times 10^7 - 6.5 \times 10^7$
temperature	±10	90−110 K	±26	$6.1 \times 10^7 - 3.6 \times 10^7$
N(^{2}D)+ O$_2$ reaction rate	±12	$3.5 \times 10^{-12} - 4.5 \times 10^{-12}$ cm^3 molecule^{-1} s^{-1}	±6	$4.4 \times 10^7 - 5.0 \times 10^7$
O(^{1}D) + O$_2$ quenching rate	±100	$1.0 \times 10^{-11} - 4.0 \times 10^{-11}$ cm^3 molecule^{-1} s^{-1}	±13	$3.9 \times 10^7 - 5.0 \times 10^7$
diffusion coefficient of exited atom	±20		±9	$4.33 \times 10^7 - 5.19 \times 10^7$
mole fraction of N(^{2}D) in discharge	±25	$3.0 \times 10^{-5} - 5.0 \times 10^{-5}$	±25	$3.5 \times 10^7 - 5.9 \times 10^7$

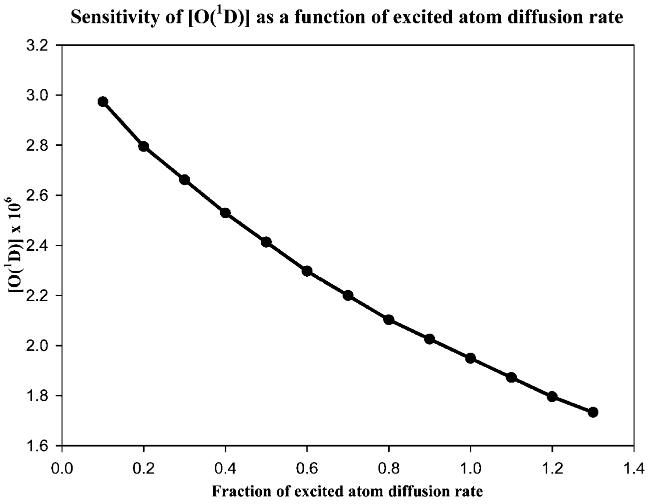

Figure 15. [O(^{1}D)] dependence on diffusion rates. Diffusion rates from this figure were changed fractionally from the following values: O(^{1}D), 442 s^{-1}; N(^{2}D), 570 s^{-1}; and N(^{2}P), 487 s^{-1}. Other conditions included a pressure of 4 mTorr, a temperature of 100 K, an N(^{2}D) mole fraction of 4 × 10^{-5}, and a quench rate for O(^{1}D) by O_2 of 2.5 × 10^{-11} cm^3 molecule^{-1} s^{-1}.

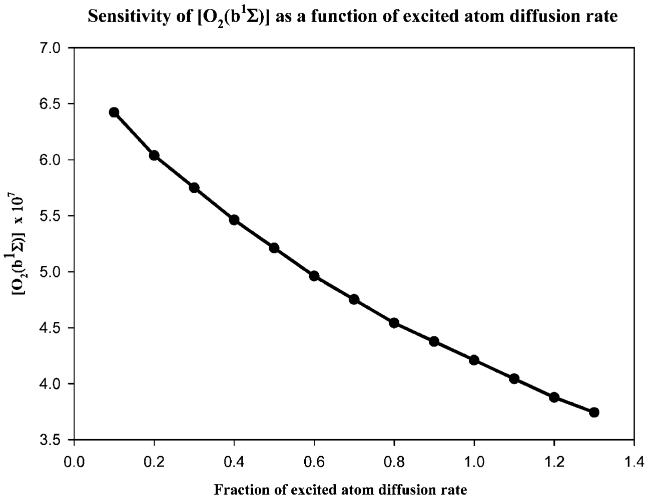

Figure 16. [O_2(b$^1\Sigma$)] dependence on diffusion rates. Diffusion rates from this figure were changed fractionally from the following values: O(^{1}D), 442 s^{-1}; N(^{2}D), 570 s^{-1}; and N(^{2}P), 487 s^{-1}. Other conditions included a pressure of 4 mTorr, a temperature of 100 K, an N(^{2}D) mole fraction of 4 × 10^{-5}, and a quench rate for O(^{1}D) by O_2 of 2.5 × 10^{-11} cm^3 molecule^{-1} s^{-1}.

VI. Conclusion

This work places an upper limit of 0.02 ± 0.02 on the branching fraction for the production of O(^{1}D) from the reaction of N(^{2}D) with O_2. This value is in good agreement with both the field analysis of Link[4] and the theoretical calculations of both González[15]and Braunstein.[16] The original interpretation[6] that a break in the vibrational distribution of the NO product at v = 8 inferred a channel to the production of O(^{1}D) is not feasible, considering the results of this paper. An alternative explanation for the vibrational distribution will be explained in a forthcoming paper on the rotational and vibrational quenching of the NO product by O_2.

Acknowledgment. The authors would like to acknowledge the essential support of Vincent Kennedy and John Cappelli in operating and maintaining the COCHISE facility during these experiments and Ramesh Sharma for valuable theoretical consultations. We would also like to thank the U.S. Air Force Office of Scientific Research for funding this research, under Task No. 2303ES/92VS04COR.

Appendix. Kinetic/Fluid Dynamical Model Used in COCHISE

A kinetic model was developed to simulate the rate of chemical reactions observed in the COCHISE reactor/spectrometer. The model incorporates a fluid dynamical analysis of the gas flow in the reaction chamber, which predicts the pressure (P) and temperature (T) of the gas on the tank centerline, based on the mass flow per inlet tube (M) and inlet tube pressure (P_i) and temperature (T_i).[17]

A schematic diagram of the flow field during COCHISE experiments is shown in Figure A1. The gas stream from each inlet tube undergoes a supersonic expansion upon entering the reaction chamber (region 1). The collision of opposing jets creates an axisymmetric stagnation zone around the tank centerline (region 2), from which the gas is then cryogenically pumped onto the chamber walls (region 3). In passing from region 1 to region 2, the gas flowing along a jet centerline traverses a plane normal shock wave (Mach disk). Therefore, the gas flow in the stagnation zone is subsonic and it may be treated as incompressible. Under these conditions, the pressure (P) at the axisymmetric stagnation point, on the tank centerline, is given by[18]

$$P = \frac{(\gamma + 1)\pi M v_t}{8(\gamma - 1)\theta_\infty^{\,2}(r - r_M)^2} \qquad \text{(A-1)}$$

where γ is the specific heat capacity ratio of the gas, r the tank cylinder radius, r_M the distance of the Mach disk from tank centerline, θ_∞ the Prandtl−Meyer maximum turning angle for the expansion of an isentropic gas into a vacuum, and v_t the terminal velocity of the supersonic jet in region 1, given by

$$v_t = \frac{\sqrt{2}\gamma R T_i}{(\gamma - 1)m} \qquad \text{(A-2)}$$

where m is the molecular weight of the gas and R is the gas constant. Because the gas flow in the inlet tubes is maintained in a laminar flow regime (Reynolds number of Re < 2300), one may neglect the effect of viscous heating in the inlet tubes and assume that the gas temperature in the stagnation zone (region 2) is equivalent to the temperature of the gas entering the inlet tubes (T_i):

$$T = T_i \qquad \text{(A-3)}$$

Under typical COCHISE operating conditions ($P \geq 4$ mTorr), the Mach disk location on the jet centerline is $r_M \geq 9$ cm. This is considerably greater than the radius of the cylindrical field of view sampled by the infrared monochromator ($r_{IR} = 1.75$ cm). Therefore, the IR chemiluminescence measured in our COCHISE experiments samples a region of bulk, thermalized gas (region 2) whose temperature and pressure (T and P) are given by eqs A-1 and A-3.

The variation in P along the tank centerline is insignificant (~1% deviation from the value of P along the jet centerlines).[7] Therefore, in developing our kinetic/fluid dynamical model for chemical reactions in COCHISE, we define a cylindrical reaction zone whose radius r_{RZ} is equivalent to r_M, and whose total volume V_{RZ} is given by

$$V_{RZ} = 4\pi d r_{RZ}^{\,2} \qquad \text{(A-4)}$$

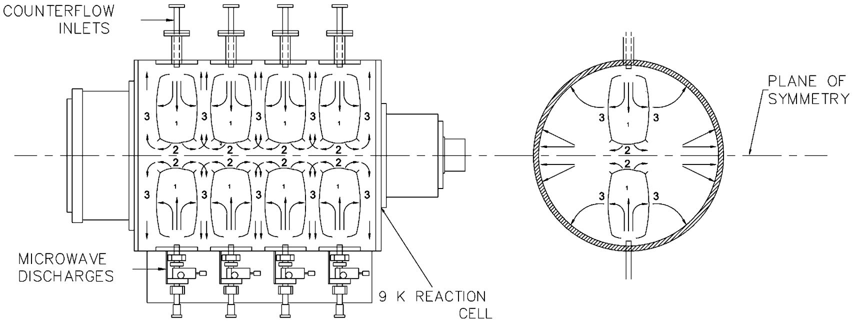

Figure A1. Schematic diagram of the COCHISE flow field.

where d is the distance between two adjacent gas inlet tubes. It is possible to calculate r_{RZ} from first principles; however, this requires exact knowledge of the cryopumping conditions in the chamber and characterization of the fluid dynamical constraints in region 3. A model to predict the sticking coefficient of gases onto cryogenically cooled surfaces has been developed by Dawson.[18] However, this model applies to the cryopumping of a stationary Maxwellian gas, a condition which is not satisfied in COCHISE experiments.[7] In the present model, therefore, r_{RZ} is determined empirically from the reaction zone pressure (P_{RZ}), which is measured 5 cm vertically above the tank centerline, in the central region of the tank (region 2). The parameter r_{RZ} is then calculated by rearranging eq A-2 and setting $P = P_{RZ}$ and $r_M = r_{RZ}$. After a reaction zone is defined via eq A-4, our kinetic/fluid dynamical model calculates the temporal evolution of a given gas species j within the reaction zone, according to the master equation:

$$\frac{\partial[j]}{\partial t} = k_f(j) - k_d(j)[j] - k_c[j] + \sum_m k_m[\alpha_m][\beta_m] - \sum_n k_n[\alpha_n][j] - \sum_o k_o[j] \quad \text{(A-5)}$$

where $[j]$ is the concentration of species j in the reaction zone; $k_f(j)$ is the zeroth-order rate of formation of species j within the reaction zone, corresponding to a constant input from the inlet tubes into the reaction zone; $k_d(j)$ and k_c are the diffusive and convective loss coefficients, respectively, for species j out of the reaction zone; k_m and k_n correspond to second-order chemical formation and destruction processes, respectively, for species j in the reaction zone; and k_o correspond to first-order loss processes of species j in the reaction zone, other than diffusion and convection (e.g., radiative quenching). The master equation is solved numerically using the Acuchem algorithm.[19] A detailed description of the individual terms contributing to this master equation is presented below.

(A) Rate of Direct Gas Input into the Reaction Zone. The density of carrier gas in a jet's free expansion region is given approximately by[7]

$$\rho = \frac{Af(\theta)M}{v_t r_i^2} \quad \text{(A-6)}$$

where r_i is the spherical radius from the exit plane of the inlet tube; A is a normalization factor; $M = 0.027$ g/s, which corresponds to 1 slpm of argon flow per inlet tube; and $f(\theta)$ is the polar angular dependence of the jet density, given by[7]

$$f(\theta) = \left[\cos\left(\frac{\pi\theta}{2\theta_\infty}\right)\right]^{2/(\gamma-1)} \quad \text{(A-7)}$$

TABLE A1: Estimated Mole Fractions of N-Atom Species in the Exit Plane of the Gas Inlet Tubes for 1% N_2/Ar Discharges[a]

species	mole fraction at inlet tube exit
$N(^4S)$	2.1×10^{-3}
$N(^2D)$	$1 \times 10^{-5}-4 \times 10^{-5}$
$N(^2P)$	$2 \times 10^{-6}-5 \times 10^{-6}$

[a] From ref 11.

The flux of carrier gas from the COCHISE inlet jets into the reaction zone can be calculated by evaluating the surface integral of the flux distributions (eqs A-6 and A-7) over the bounding surface of the reaction zone defined previously (eqs 1−4). It may then be shown that, under typical COCHISE operating conditions ($T = 100$ K, $P = 4$ mTorr), 57% of the argon carrier gas from the inlet jets enters directly into the reaction zone. This corresponds to an argon carrier gas source term in the reaction zone of $k_f(\text{Ar}) = 3.2$ mTorr/ms.The source terms for all other species in the COCHISE reaction zone are evaluated according to their expected mole fraction upon exiting the gas inlet tubes. The values used for N atoms (ground state and electronically excited) are based on direct observations of discharge effluents in a flow reactor at the same flow rate and discharge pressure conditions as these COCHISE experiments, but at room temperature (Table A1).[2,20]

(B) Diffusive Losses. The diffusive loss rate constants, $k_d(j)$, are calculated by assuming irreversible loss of diffusing species upon reaching the bounding surface of the reaction zone (i.e., no "re-crossing" of species back into the reaction zone after they exit it). In this case, $k_d(j)$ is given by[21]

$$k_d(j) = D_{j\alpha}\left[\left(\frac{\pi}{4d}\right)^2 + \frac{5.81}{r_{RZ}^2}\right] \quad \text{(A-8)}$$

where $D_{j\alpha}$ is the binary diffusion coefficient for species j in a bath of gas α, diffusing irreversibly out from a cylindrical volume of length $4d$ and a cross-sectional area of πr_{RZ}^2. Because of the lack of experimental characterizations of diffusion parameters for chemical species and conditions relevant to COCHISE experiments, our kinetic model relied on calculation of most of these parameters from first principles and/or extrapolation of values measured at room temperature to the cryogenic conditions present in the COCHISE reactor.

For the simple case of hard-sphere collisions, the binary diffusion coefficient, $D_{j\alpha}$, may be calculated from the rigorous kinetic theory of gases, as[14]

$$D_{j\alpha} = \left(\frac{3}{16\rho d_{j\alpha}{}^2}\right)\sqrt{\frac{2RT}{\pi\mu_{j\alpha}}} \quad \text{(A-9)}$$

where ρ is the number density of the bath gas, $\mu_{j\alpha}$ is the reduced mass of species j and α, and $d_{j\alpha}$ is the average atomic or

TABLE A2: Diffusion Coefficients at $T = 100$ K in an Argon Bath Gas

diffusing species	diffusion coefficient at $T = 100$ K (cm^2 mTorr s^{-1})	reference
Ar	17 500	Hirschfelder et al.[16] (Table 1.2-2)
O_2, $O_2(b^1\Sigma)$	19 200	our estimate, based on Lennard-Jones interaction parameters from Maitland et al.[17]
$N(^4S)$	44 200	our estimate, based on $N(^2D)$ value scaled by relative diffusion coefficients of $N(^4S)$ and $N(^2D)$ in N_2 bath gas[11]
$N(^2D)$	36 000	Lin and Kaufman[26]
$N(^2P)$	30 700	Ianuzzi and Kaufman[27]
$O(^3P)$	27 900	Morgan and Schiff[28]
$O(^1D)$	27 900 (upper limit)	no experimental data available; value arbitrarily set equal to the $O(^3P)$ diffusion coefficient
NO(Π,v,J)	21 200	Our estimate, based on Ar diffusion coefficient scaled by NO/Ar reduced mass and collision cross section[21]

molecular diameter of the colliding species j and α. Equation A-9 may also be used to calculate self-diffusion coefficients (D_α) by simply substituting the molecular weight (m_α) and diameter (d_α) for $\mu_{j\alpha}$ and $d_{j\alpha}$, respectively.

However, a more sophisticated approach is required to calculate diffusion coefficients at cryogenic temperatures, because of the significant role played by intermolecular attractive forces under those conditions. Numerous theories have been developed to account for this effect.[22,23] A common method, known as the Chapman−Enskog formalism, enables precise calculation of transport properties of gases, provided that the intermolecular pair potential between the colliding atoms or molecules is known. If a Lennard-Jones 6−12 interaction potential is assumed, the binary diffusion coefficient for species j diffusing through a bath gas α is given by[14]

$$D_{j\alpha} = \left(\frac{3}{16\rho\sigma_{j\alpha}^2}\right)\left(\frac{1}{\Omega^*_{j\alpha}}\right)\sqrt{\frac{2RT}{\pi\mu_{j\alpha}}} \qquad \text{(A-10)}$$

where $\sigma_{j\alpha}$ is the Lennard-Jones collision diameter. $\Omega^*_{j\alpha}$, which is the reduced collision integral, incorporates the effect of intermolecular forces and is dependent on temperature and on the Lennard-Jones interaction energy, or well depth ($\epsilon_{j\alpha}$), between species j and α. At $T = 300$ K, $\Omega^*_{j\alpha}$ is normally very close to unity (within 5%) and eq A-10 reduces to the simple hard-sphere collision expression given in eq A-9.[13] However, at cryogenic temperatures, $\Omega^*_{j\alpha} > 1$ and the diffusion coefficient $D_{j\alpha}$ becomes significantly smaller than that predicted by the hard-sphere model. For nonpolar gases interacting via an attractive $U(r) = -C_6/r^6$ potential (Lennard-Jones 6−12), $D_{j\alpha}$ can be shown to exhibit a $T^{11/6}$ temperature dependence (as opposed to the slower $T^{3/2}$ dependence predicted by eq A-8).[14] In this particular case, diffusion coefficients calculated using eq A-10 for typical COCHISE reaction zone conditions ($T = 100$ K) would be 30% lower than that predicted via a simple hard-sphere model (eq A-9).

The self-diffusivity of argon at cryogenic temperatures has been determined empirically and, thus, serves to illustrate the validity of the Chapman−Enskog formalism described previously. At $T = 100$ K, the experimentally measured value of $D_{Ar} = 17\,500$ mTorr cm^2 s^{-1}.[13] This agrees well with an extrapolation of the experimentally determined $D_{Ar}(300\text{ K})$ via a $T^{11/6}$ dependence, which yields $D_{Ar}(100\text{ K}) = 18\,900$ mTorr cm^2 s^{-1}. Thus, the self-diffusivity of argon at cryogenic temperatures is well-described (within an accuracy of 10%) by the Chapman−Enskog model for nonpolar gases interacting via a Lennard-Jones 6−12 potential. By contrast, a hard-sphere collision model calculation based on $d_{Ar} = \sigma_{Ar} = 3.35$ Å (ref 5) predicts $D_{Ar}(100\text{ K}) = 28\,300$ mTorr cm^2 s^{-1}. This large discrepancy illustrates the tendency for significant reduction in diffusion coefficients at low temperatures due to the intermolecular force effect.

The chemical species of interest in our COCHISE experiments are Ar, O_2, $O_2(b^1\Sigma)$, $N(^4S)$, $N(^2D)$, $N(^2P)$, NO(Ω,v,J), $O(^3P)$, and $O(^1D)$. Table A2 lists the diffusion coefficients of these species under COCHISE reaction conditions, based on an extrapolation of measured room-temperature values via a $T^{11/6}$ dependence (with the exception of Ar, for which $D_{Ar}(100\text{ K})$ has been experimentally determined).

The Lennard-Jones collision diameters of Ar and O_2 are almost identical ($\sigma_{Ar} = 3.35$ Å; $\sigma_{O_2} = 3.38$ Å). However, the attractive potential well depth is slightly larger for Ar/Ar interactions ($\epsilon_{Ar,Ar} = 12.15$ meV) than for O_2/Ar and O_2/O_2 collisions ($\epsilon_{O_2,Ar} = 11.5$ meV and $\epsilon_{O_2,O_2} = 10.8$ meV).[5] According to the Chapman−Enskog formalism, this should result in a 10% higher diffusion coefficient for O_2/Ar than for Ar/Ar at $T = 100$ K (see Table A2). This is consistent with the experimentally determined value of the self-diffusion coefficient of O_2 at $T = 100$ K, which is 15% larger than $D_{Ar}(100\text{ K})$.[13,24,25]

The diffusion coefficients listed in Table A2 correspond to the case of a pure argon bath gas at $T = 100$ K. In the present COCHISE experiments, the O_2:Ar mixing ratio in the reaction zone is close to 1:1. Because of the similarity in interaction potentials between Ar and O_2 species, this change in bath gas composition does not significantly affect the diffusion of inert species through this medium (e.g., the diffusion coefficients of O_2 and Ar themselves will change by <5%).[13] However, atomic species that interact strongly with O_2 (e.g., electronically excited N and O atoms) may have substantially lower diffusion rates under high O_2 mole fraction conditions. It is beyond the scope of this paper to estimate these effects accurately. A sensitivity analysis is therefore presented, to ascertain the range of variability introduced into our kinetic model by the added uncertainty in diffusion parameters under high O_2 mole fraction conditions.

The diffusion properties of metastable N atoms in Ar at $T = 300$ K are fairly well-established experimentally.[8,15,16] However, to our knowledge, no such information is available for metastable O atoms. Therefore, our kinetic model utilizes the experimentally determined diffusion coefficient of ground-state O atoms as an upper limit for the diffusion coefficients of $O(^1D)$. The actual values are expected to be 10%−30% lower than this;[6] we explore the effect of this uncertainty in the sensitivity analysis section below.

On the basis of these parameters, the argon carrier gas diffusion rate coefficient under typical COCHISE operating conditions ($T = 100$ K, $P = 4$ mTorr) can be shown to be $k_d(\text{Ar}) = 340$ s^{-1}. This value corresponds to a diffusion half-life of $\tau_d(\text{Ar}) = 2.0$ ms out of the reaction zone.

(C) Convective Losses. The rate of convective loss of gases from the COCHISE reaction zone is calculated by considering the conservation of linear momentum of the jet gas plumes along a plane perpendicular to the jet directions. The mass flow rates in opposing jets in COCHISE experiments are set to achieve momentum balance along the jet centerlines. However, any momentum component perpendicular to a jet centerline will be imparted onto the thermalized reaction zone, thereby displacing it vertically toward the top (and bottom) walls of the COCHISE reaction chamber. It may then be shown, by a simple Newtonian balance of forces argument, that the convective loss coefficient (k_c) for all species in the reaction zone is given by

$$k_c = \frac{\langle v_i \rangle}{\sqrt{r_{RZ}^2}} \qquad \text{(A-11)}$$

where $\langle v_i \rangle$ is the component of gas jet velocity perpendicular to the jet centerline, averaged over all polar angles $-\theta_{max} < \theta < \theta_{max}$ for which the expanding gas jet traverses the COCHISE reaction zone defined previously (eq A-3). θ_{max} is defined as

$$\tan \theta_{max} = \frac{r_{RZ}}{z_0} \qquad \text{(A-12)}$$

where $z_0 = 20.5$ cm is the distance between the inlet tube gas source and the COCHISE reaction cell centerline. The parameter $\langle v_i \rangle$ may be calculated from the angular dependence of the gas flow in an isentropic, supersonic expansion of a gas into vacuum; it is given by the relation

$$\langle v_i \rangle = (1 - \cos \theta_{max}) v_t \qquad \text{(A-13)}$$

The convective loss coefficient, k_c, is independent of the chemical identity of species j in the reaction zone. At $T = 100$ K and $P = 4$ mTorr, it may be shown that $k_c = 175\ s^{-1}$, rendering a convective loss half-life of $\tau_c = 4.0$ ms.

(D) Quenching Rates (Radiative and Collisional). The radiative lifetimes of O(^{1}D) metastables are well-established. O(^{1}D) may decay via 630-nm emission with a radiative lifetime of 148 s.[29]

For collisional quenching of atomic metastable species to be of significant magnitude, a resonant or complex-forming mechanism is required. Collisions with the Ar bath gas ($k < 5 \times 10^{-13}$ cm^3 molecule^{-1} s^{-1})[30] can therefore be ignored, because the interaction of this inert gas with atomic metastables is purely physical. Collisions of O(^{1}D) with O_2, on the other hand, proceed via an excited O_3 intermediate and are thus highly efficient channels for electronic quenching of these electronically excited species. The room-temperature rate coefficient for the quenching of O(^{1}D) by O_2 is $k = 4.0 \times 10^{-11}$ cm^3 molecule^{-1} s^{-1}. The reaction has a very weak negative temperature dependence, and its expected value at COCHISE operating temperatures lies in the range of $k(100\ K) = 0.2 \times 10^{-10}-1.8 \times 10^{-10}$ cm^3 molecule^{-1} s^{-1}.[13] Our models use a lower-end value of 2.5×10^{-11} cm^3 molecule^{-1} s^{-1} for this reaction, to avoid overpredicting the expected [O_2(b$^1\Sigma$)] value.

References and Notes

(1) Sharp, W. E.; Rees, M. H.; Stewart, A. I. *J. Geophys. Res.* **1979**, *84* (A5), 1977.

(2) Rusch, D. W.; Gerard, J.-C.; Sharp, W. E. *Geophys. Res. Lett.* **1978**, *5*, 1043.

(3) Torr, D. G.; Richards, P. G.; Torr, M. R. *Geophys. Res. Lett.* **1980**, *7* (5), 410−412.

(4) Link, R.; Swaminathan, P. K. *Planet. Space Sci.* **1992**, *40*, 699−705.

(5) Kennealy, J. P.; DelGreco, F. P.; Caledonia, G. E.; Green, B. D. *J. Chem. Phys.* **1979**, *69*, 1574.

(6) Rawlins, W. T.; Fraser, M. E.; Miller, S. M. *J. Phys. Chem.* **1989**, *93*, 1097−1107.

(7) Rawlins, W. T.; Murphy, H. C.; Caledonia, G. E.; Kennealy, J. P.; Robert, F. X.; Corman, A.; Armstrong, R. A. *Appl. Opt.* **1984**, *23*, 3316−3324.

(8) Lee, L. C.; Slanger, T. G. *J. Chem. Phys.* **1978**, *69*, 4053−4060.

(9) Rawlins, W. T.; Fraser, M. E.; Miller, S. M.; Blumberg, W. A. M. *J. Chem. Phys.* **1992**, *96*, 7555.

(10) NIST Atomic Spectra Database, http://ww.physics.nist.gov/cgi-bin/Atdaa/main-asd.

(11) Huestis, D. L. Radiative Transition Probabilities. In *Atomic, Molecular, and Optical Physics Handbook*; Drake, G. W. F., Ed.; AIP Press: Woodbury, NY, 1996.

(12) Slanger, T. G.; Wood, B. J.; Black, G. *J. Geophys. Res.* **1971**, *76* (34), 8430−8433.

(13) DeMore, W. B.; Sander, S. P.; Howard, C. J.; Ravishankara, A. R.; Golden, D. M.; Kolb, C. E.; Hampson, R. F.; Kurylo, M. J.; Molina, M. J. Chemical Kinetics and Photochemical Data for Use in Stratospheric Modeling, Evaluation Number 12. *JPL Publ.* **1997**, *97-4*.

(14) Phillips, C. M.; Steinfeld, J. I.; Miller, S. M. *J. Phys. Chem.* **1987**, *91*, 5001.

(15) González, M.; Miquel, I.; Sanyos, R. *Chem. Phys. Lett.* **2001**, *335*, 339−247.

(16) Braunstein, M.; Duff, J. W. *J. Chem. Phys.* **2000**, *113* (17), 7406−7413.

(17) Caledonia, G. E.; Green, B. D.; Simmons, G. A.; Kennealy, J. P.; Robert, F. X. Corman, A.; Delgreco, F. P. AFGL-TR-77-0281, 1977, Environmental Research Papers, No. 619.

(18) Dawson, J. P. *J. Spacecr. Rockets* **1966**, *3*, 218.

(19) Braun, W.; Herron, J. T.; Kahaner, D. K. *Int. J. Chem. Kinet.* **1988**, *20*, 51.

(20) Rawlins, W. T.; Piper, L. G.; Fraser, M. E.; Murphy, H. C.; Tucker, T. R.; Gelb, A. USAF Report No. PSI-9032/TR-901, 1989.

(21) Cunningham, R. E.; Williams, R. J. J. *Diffusion in Gases and Porous Media*; Plenum Press: New York, 1980.

(22) Hirschfelder, J. O.; Curtiss, C. F.; Byrd, R. B. *Molecular Theory of Gases and Liquids*, 3rd ed.; Wiley: New York, 1966.

(23) Maitland, G. C.; Rigby, M.; Smith, E. B.; Wakeham, W. A. *Intermolecular Forces: Their Origin and Determination*, 2nd ed.; Oxford University Press: Cambridge, U.K., 1987.

(24) Winn, E. B. *Phys. Rev.* **1950**, *80*, 1024.

(25) Winter, E. R. S. *Trans. Faraday Soc.* **1951**, *47*, 342.

(26) Lin, C.-L.; Kaufman, F. *J. Chem. Phys.* **1971**, *55* (8), 3760.

(27) Ianuzzi, M. P.; Kaufman, F. *J. Chem. Phys.* **1980**, *73* (9), 4701.

(28) Morgan, J. E.; Schiff, H. I. *Can. J. Chem.* **1964**, *42*, 2300.

(29) Wiese, W. L.; Smith, M.; Glennon, B. M. Atomic Transition Probabilities, Vol. I; National Standard Reference Data System Report NRRDS-NBS-4, 1966.

(30) Shi, J.; Barker, J. R. *Int. J. Chem. Kinet.* **1990**, *22*, 1283.